

# We are IntechOpen, the world's leading publisher of Open Access books Built by scientists, for scientists

6,900

Open access books available

186,000

International authors and editors

200M

Downloads

Our authors are among the

154

Countries delivered to

TOP 1%

most cited scientists

12.2%

Contributors from top 500 universities



WEB OF SCIENCE™

Selection of our books indexed in the Book Citation Index  
in Web of Science™ Core Collection (BKCI)

Interested in publishing with us?  
Contact [book.department@intechopen.com](mailto:book.department@intechopen.com)

Numbers displayed above are based on latest data collected.  
For more information visit [www.intechopen.com](http://www.intechopen.com)



---

# **Simulation and Optimization of Electrical Insulation in Power Quality Monitoring Sensors Applied in the Medium-Voltage**

---

Sender Rocha dos Santos, Rodrigo Peres,  
Wagner Francisco Rezende Cano and  
Joao Batista Rosolem

Additional information is available at the end of the chapter

<http://dx.doi.org/10.5772/intechopen.77187>

---

## **Abstract**

Thanks to the Smart Grid initiative, the focus for medium-voltage MV (13.8–34 kV) smart meters leveraged the development of sensors for distribution application. In order to be useful at power quality monitoring, the sensors needs to attend, at least, the International Electrotechnical Commission (IEC) 61000–4-30 and IEC 61000–4-7 standards with high-accuracy in terms of voltage (less than 0.1%), current (less than 1.0%) and measuring the waveform distortion data up to the 50th harmonic of 50 or 60 Hz alternating frequency. This kind of sensor is built with two capacitors connected in series. The first capacitor is a commercial electronic low-voltage device. One terminal of this capacitor is connected to the medium-voltage (MV) conductor. The second one, is connected to the other capacitor that is constructed using the own sensor packaging. This second capacitor has an electrode, that is connected with the first capacitor and the other terminal is connected to the ground. The voltage is measured between the terminals of the low voltage capacitor. The performance of this capacitor depends on the geometry and the materials used in the electrical insulation. This chapter describes the simulations and modeling of the capacitor electrodes using a finite-elements software, COMSOL Multiphysics, for modeling in order to optimize the performance of sensor in terms of electric field distribution.

**Keywords:** simulation, electrical insulation, sensors, power quality monitoring, medium-voltage, capacitive divider

---

## 1. Introduction

One of the fundamentals of the Smart Grid concept is that user safety should be ensured while monitoring, updating and continuously reliably distributing electricity grid by adding smart meters and monitoring systems to the power grid is obtained. This is necessary in order to ensure electronic communication between suppliers and consumers [1]. Smart grid monitoring systems require various types of sensors and transducers to monitor the grid conditions. After the Smart Grid initiative, the focus for medium-voltage (MV) smart meters leveraged the development of energy quality sensors for distribution application [2]. In order to be useful at power quality monitoring, the sensors need to attend at least the International Electrotechnical Commission (IEC) 61000-4-30 and IEC 61000-4-7 standards [3, 4] with high-accuracy in terms of voltage (less than 0.1%), current (less than 1.0%) and measure waveform distortion data up to the 50th harmonic. In addition, this sensor must be easy to install and remove without disconnect the distribution network and it must monitor the grid for a period that may last longer than 1 week.

In this context, two power quality-monitoring technologies are prominent: wireless sensors [5] or optical fiber sensors [6, 7]. Wireless sensors have the advantage of not needing any physical medium to transmit the data to a remote measuring unit, but need to use batteries in order to keep the electronic circuits working. On the other hand, optical fiber sensors have the advantage of no need for electrical powering, but they need a physical link to the remote measuring unit.

Independently of the technologic choice, current and voltage waves have to be measured in the medium-voltage (MV) in order to obtain the power quality parameters. Particularly, for voltage measurements, a capacitive or a resistive circuit divider [8–10] can be used to obtain a voltage sample of the MV conductor. In this work, it is analyzed the capacitive case. The low capacitance of this circuit accumulates more than 99.9% of the total voltage (e.g. 13.8 or 34 kV) and is totally constructed using the own sensor packaging. In this capacitive circuit the first capacitor is a commercial electronic low-voltage (LV) device. One terminal of this capacitor is connected to the medium-voltage conductor. The second one, is connected to the other capacitor that is constructed using the own sensor packaging. This second capacitor has an electrode, that is connected with the first capacitor and the other terminal is connected to the ground.

A rigorous design is necessary for these sensors considering the safety aspects regarding to the technician activities and to some environmental effects that can influence their performance, such as, temperature, pressure and wind. Besides, it should be taken into account that the external elements in the proximities of the sensors can alter the electrical and magnetic field acting inside of them.

The current sensor for power quality measurements was not evaluated in this work since its operation is different from the voltage sensor and in general it does not affect the insulation properties of the power quality sensor. Traditional devices used as current sensor are current transformer or Rogowski coil [11], and they are connected direct to the MV conductor without ground connection.

This chapter is organized as follows. Section 2 describes the physical structure of the sensor studied in this work. Section 3 describes the analytical modeling of the sensor. Section 4 describes the finite-element method (FEM) review mainly focused in simulation of an electrostatic field and the sensor. In addition in this section it is presented the sensor simulation validation. Finally, Section 5 presents the conclusions.

## 2. Voltage sensor for power quality applications

The proposed case study was the modeling of a current and voltage sensor for MV applications to be applied in live lines for the evaluation of energy quality.

According to **Figure 1**, a capacitive divider represented by  $C_1$  and  $C_2$  (F) provides the voltage measurement. The capacitor  $C_1$  is a commercial capacitor used in electronic applications and is placed in an electronic board of the sensor.  $C_2$  is a capacitor formed by an electrode and a grounded pipe isolated by an insulation material (such as polymer, ceramic, glass or oil-impregnated paper) where a high-intensity electric field remains concentrated. To meet accuracy of less than 0.5% in the voltage measurements, it is necessary to connect the LV terminal of the sensor to the ground. Thus, it is not possible to use the parasitic capacitance as the  $C_2$

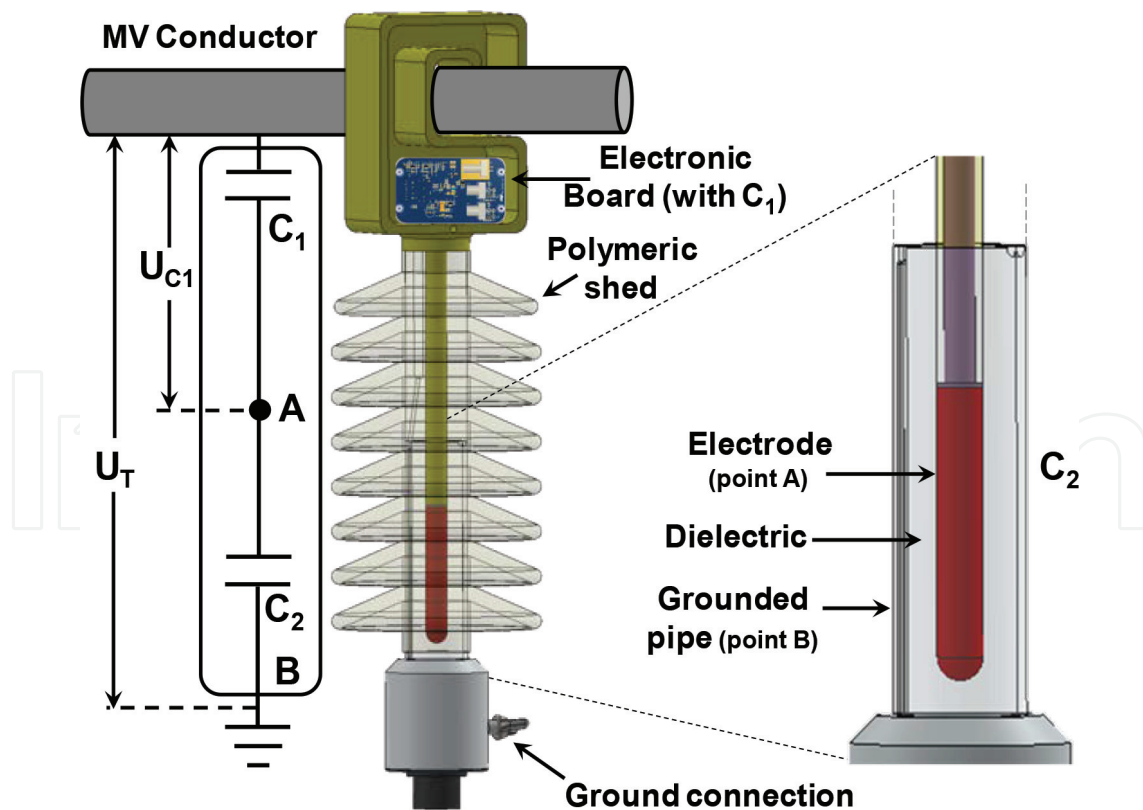


**Figure 1.** The voltage sensor for power quality applications. In the right is shown the elements that create the capacitance  $C_2$ .

capacitor. The capacitive divider is designed in such way that  $C_2$  retains practically the totally line voltage. The voltage on  $C_1$  measured by the sensor is defined by:

$$U_{C_1} = U_T \frac{C_2}{(C_1 + C_2)} \approx U_T \frac{C_2}{C_1} \quad (1)$$

where  $U_T$  (V) is the total voltage. The approximation in Eq. (1) is valid when  $C_1 \gg C_2$ .

The maximum voltage concentrated in  $C_1$  is around 5 V. The line voltage in MV can be 1 or 35 kV according [12]. Examples of voltage classifications between these values are: 4.16, 12.47, 13.2, 13.8, 24.94 and 34.5 kV.

The  $C_2$  design must meet some important requirements, such as, adequate dielectric strength to support pulse voltage up to 100 kV [13], homogeneous field electric around the electrode and absence of air bubbles near the electrode interface in order to reduce the growing of partial discharges in the sensor [14]. The growing of partial discharges in the insulation due to electric field concentration in a specific place and over time causes premature aging and breakdown of insulation systems [15–19].

The dimensions of the sensor and characteristics of the insulation material will be described in Section 3.

### 3. Capacitive analytical modeling for power quality sensor

The basic reference structure adopted for the voltage sensor is composed of two coaxial cylinders terminated in hemispheres, as shown in **Figure 2**. This type of geometry simplifies the practical construction of  $C_2$  and allows the creation of an analytical model. The internal electrode is at line potential ( $U$ ) and the external electrode is in the earth potential (0 V). The internal and external electrode radii are, respectively,  $a$  (mm) and  $b$  (mm), the electrical permittivity of the medium is  $\varepsilon$  and the cylinder length is  $L$  (mm). It should be noted that there is no region of electric flux dispersion through the upper horizontal line due to the presence of a guard's electrode not shown in the figure. This figure also shows an equipotential line defined by the distance  $x$  whose origin is the longitudinal axis of the cylinders. The equipotential line has a value exact in the region between the cylinders because the electric field in this region is constant and uniform while the equipotential in the hemispheres region has a value approximated because the electric field is non-uniform. As shown in [20], the equipotential surface tends toward a hemisphere and by heuristic approach this is a good approximation.

The analytical study demonstrates the optimum relation between the radii of the cylinders. The electric field is radial and is given by [21]:

$$E(x) = \frac{q}{2\pi L x \varepsilon} \quad (2)$$

where  $q$  (C) is the charge on the cylindrical part of the central electrode. The integral of the electric field between the electrodes provides the voltage  $U$  between them, i.e.:

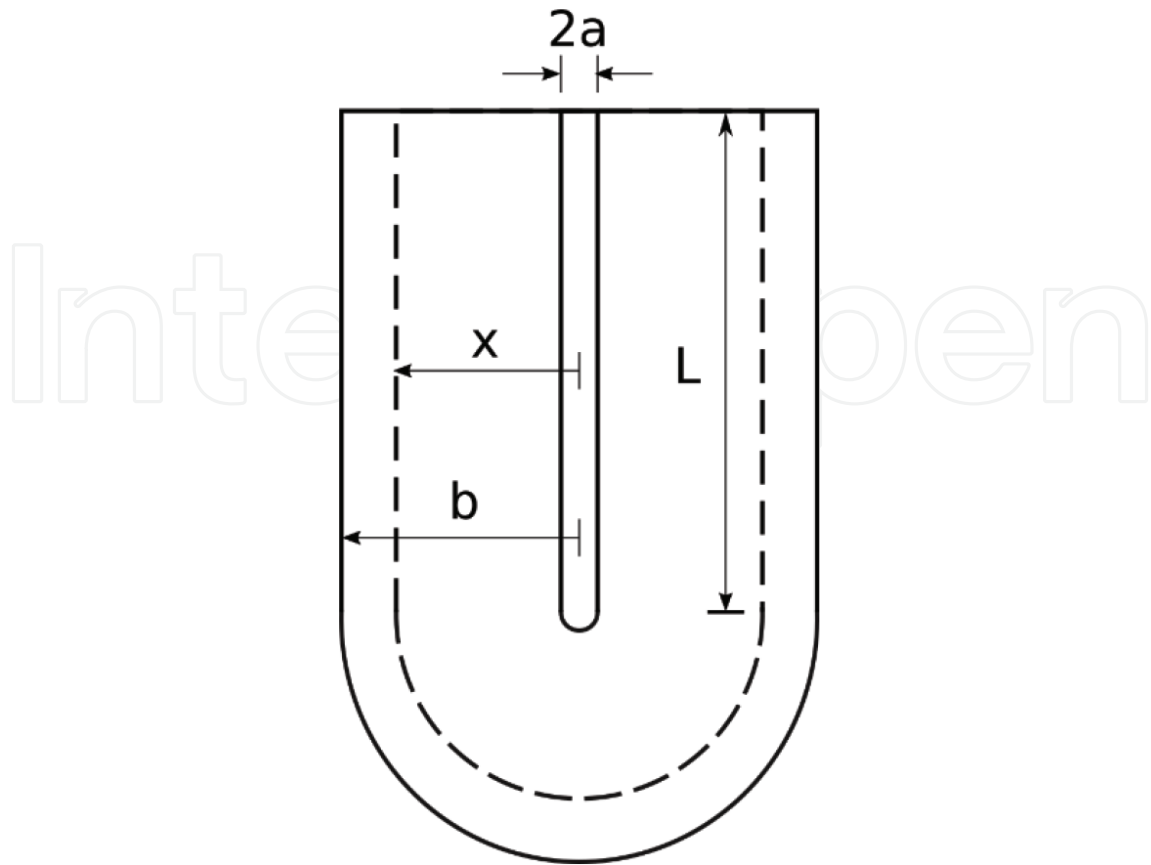


**Figure 2.** Structure of voltage sensor and equipotential surface. Dimension of geometric parameters in millimeters.

$$U = \int_a^b E(x)dx = \frac{q}{2\pi L\epsilon} \ln\left(\frac{b}{a}\right) \quad (3)$$

Substituting  $q$  from Eq. (3) into Eq. (2) leads to:

$$E(x) = \frac{U}{\ln\left(\frac{b}{a}\right)} \frac{1}{x} \quad (4)$$

where, substituting  $x$  to  $a$ , being  $a \ll b$ , it is evident that the maximum value of the electric field occurs on the surface of the internal electrode. This maximum field value is given by [22]:

$$E_{max} = \frac{U}{\ln\left(\frac{b}{a}\right)} \frac{1}{a} \quad (5)$$

It is emphasized that the maximum value of the electric field is of interest in the design of the sensor, since it determines the beginning of the insulation rupture process through the dielectric. An analysis of Eq. (5) shows that this maximum field tends to infinity for the boundary conditions  $a \rightarrow 0$  and  $a \rightarrow b$ . The first case refers to an extremely fine internal electrode, where the electric field on its surface is extremely high. The second case tends to an infinitesimal distance between the electrodes, which has to withstand voltage. Therefore, it is clear that there is at least one minimum region between these two conditions, which is the optimal condition for

the design of the sensor. Given  $b$ , the minimum value of  $E_{max}(a)$  can be obtained by differentiating the maximum field with respect to  $a$  and making this result equal to zero:

$$\frac{dE_{max}(a)}{da} = 0 \quad (6)$$

what provides the optimal condition:

$$\frac{b}{a} = e \quad (7)$$

where  $e = 2.718$  is the basis of natural logarithms. Therefore, the dimensioning of the electrodes should be such that the ratio of the radii of the internal and external electrode obeys the Eq. (7). Taking the condition of Eq. (7) into Eq. (5) it is obtained:

$$E_{max} = \frac{U}{a} \quad (8)$$

**Figure 3** shows the behavior of the maximum electric field for an external electrode of  $b = 50 \text{ mm}$  of radius and different radii for the internal electrode when a voltage of 100 kV is applied between the electrodes. It is observed that the minimum region is obtained by Eq. (7), where  $a = 18.4 \text{ mm}$ . It is also noted in **Figure 3** that the electric field variation around the minimum value is very small, such as small variations around the optimum relation expressed in Eq. (7) do not compromise the design. It should be noted that the critical region for the rupture of the dielectric occurs in the hemispheric region, however this region can be

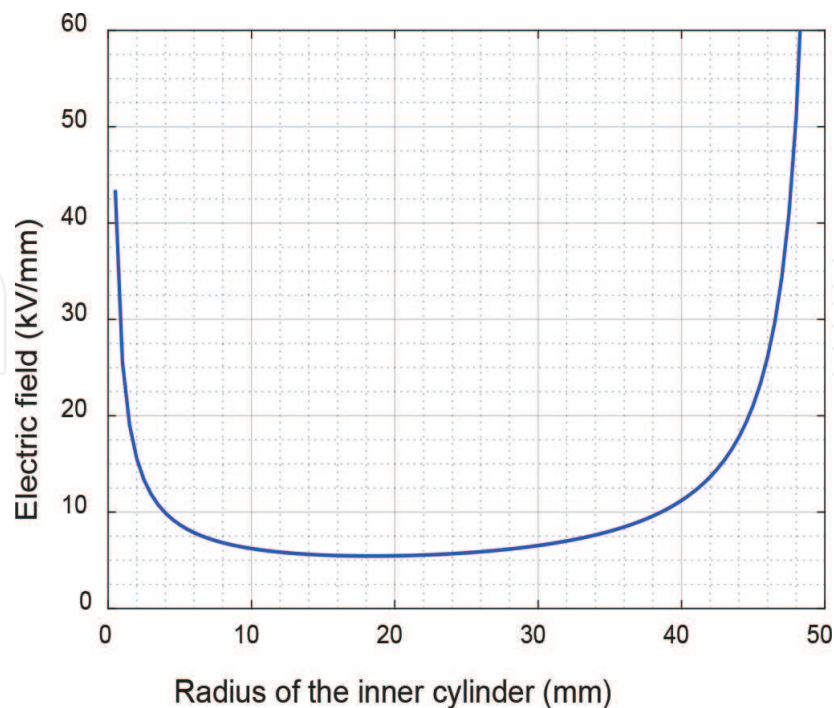


**Figure 3.** Electrical field on the surface of the internal electrode ( $0 < a < b$ ), for  $b = 50 \text{ mm}$  and  $U_T = 100 \text{ kV}$ .

elongated, increase the radius of the center electrode, tending to a revolution ellipsoid in an attempt to reduce the electric field at the electrode surface. These variations could be evaluated through COMSOL Multiphysics software.

As discussed earlier, the hemispheric region may be modified in order to attenuate the electric field at the tip surface of the central electrode. However, this makes analytical modeling difficult, and therefore the numerical calculations become necessary. For the purpose of analytical calculations, the hemispheric configuration for the electrodes (internal and external) is assumed, according to **Figure 2**. In the region between the hemispheres, the electric field is radial and could be described as follows:

$$E(x) = \frac{q_h}{2\pi x^2 \epsilon} \quad (9)$$

where  $q_h$  (C) is the charge on the hemispheric part of the central electrode. The integral of the electric field between the electrodes provides the voltage between them:

$$U = \int_a^b E(x) dx = \frac{q_h}{2\pi \epsilon} \left( \frac{1}{a} - \frac{1}{b} \right) \quad (10)$$

Substituting  $q_h$  from Eq. (10) into Eq. (9) gives:

$$E(x) = \frac{Uab}{(b-a)x^2} \quad (11)$$

In a similar way to the case of the cylinder, the maximum field occurs on the surface of the electrode:

$$E_{max} = \frac{Ub}{a(b-a)} \quad (12)$$

Differentiating Eq. (6) with respect to  $a$  and making this result equal to zero, the minimum of this function occurs for the condition:

$$b = 2a \quad (13)$$

**Figure 4** shows the electric field on the surfaces of the cylinder and the hemisphere, for different values of the  $a/b$  ratio. It is observed that the minimum field of the hemisphere occurs for  $a/b = 0.5$  as showed by Eq. (13). The modification of the cylinder termination, passing from a flat half ellipsoid of revolution to a hemisphere and to a stretched half ellipsoid of revolution, aims to optimize the electric field on this region considering the cylindrical region as a reference. This can be done taken into account Equation 7. The dimensions of the ellipsoid could be obtained through FEM developed in the COMSOL Multiphysics software.

The capacitance between the electrodes can be easily calculated by integrating the electric flux along the spatial surface defined in **Figure 3** resulting in:

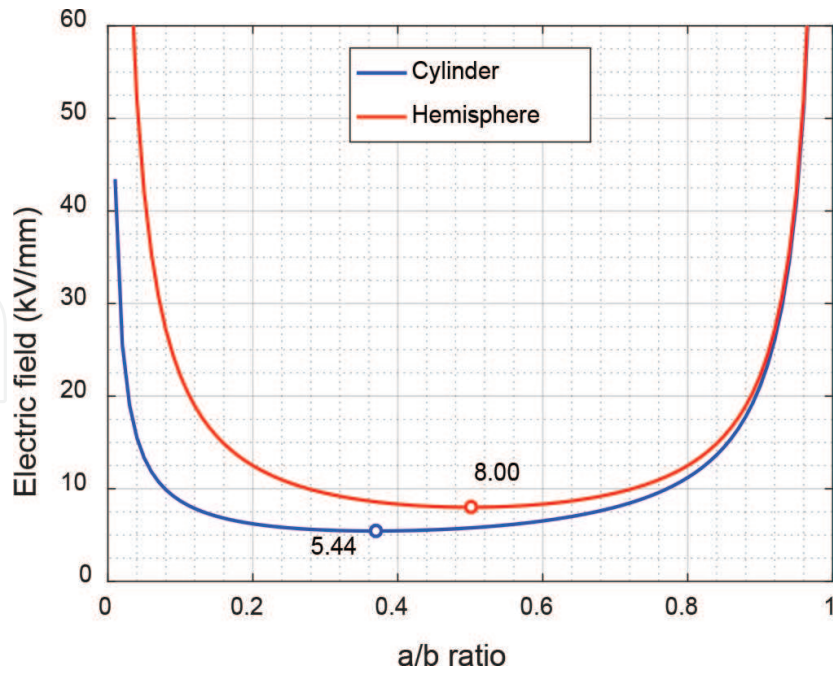


**Figure 4.** Electric field on the surface of the internal electrode, for  $b = 50 \text{ mm}$  and  $U = 100 \text{ kV}$ . The marks indicate minimum values on the surfaces of the cylinder and the hemisphere, for different values of the  $a/b$  ratio.

$$C = 2\pi\epsilon \left[ \frac{L}{\ln\left(\frac{b}{a}\right)} + \frac{ab}{(b-a)} \right] \quad (14)$$

By inserting the condition of Eq. (7) into Eq. (14) one obtains:

$$C = 2\pi\epsilon \left[ L + \frac{ae}{(e-1)} \right] \quad (15)$$

This can also be expressed as:

$$C = 0.0556\epsilon_r [L + 1.58a] \quad (16)$$

where  $\epsilon_r$  is the relative permittivity of the medium and the capacitance  $C$  is obtained in pF for  $L$  and  $a$  in millimeters. For example, considering  $\epsilon_r = 3.8$  (acetal, dielectric strength  $>50 \text{ kV/mm}$ , DIN 53481 [23]),  $L = 50 \text{ mm}$ , and  $a = 18.4 \text{ mm}$  ( $b = 50 \text{ mm}$ ),  $C = 16.7 \text{ pF}$  is obtained.

It is observed that the minimum field of the hemisphere occurs for  $a/b = 0.5$ .

#### 4. FEM review and simulation validation

FEM is based on the solution of a boundary value problem composed of a governing equation and boundary conditions. The main idea behind this method is the division of the domain of interest in subdomains known as elements and the adoption of shape functions for the

unknown variables, which are only solved for the nodes (element corners). Thus, instead of solving an analytical equation, these unknowns are determined by a set of algebraic equations and the results for regions other than the nodes can be obtained by interpolation. Proper domain discretization is crucial to ensure the accuracy of results since the mesh format must adequately reproduce the original geometry of the structure. An example of domain discretization can be seen in **Figure 5**.

This procedure reduces the generality of the mathematical framework, but enables the study of components of complex geometry. Many real world study cases involve the analysis of such problems, which are virtually impossible to be done by analytical methods.

A succinct overview of FEM for the simulation of an electrostatic field is presented next considering a stationary solving method since the voltage boundary condition chosen has a constant value. A more detailed explanation can be found in [24–28]. The voltage distribution in a dielectric of arbitrary geometry is described by the following differential equation:

$$\nabla \cdot (\epsilon_0 \epsilon_r \mathbf{E}) = \rho_v \tag{17}$$

where  $\epsilon_0 = 8.85419 \times 10^{-12} \text{ F/m}$ ,  $\epsilon_r$  is the relative permittivity,  $E$  (kV/mm) is the electric field and  $\rho_v$  ( $\text{C/m}^3$ ) is the free charge density. The relation between electric field and the voltage  $U$  is defined as:

$$-\nabla U = E \tag{18}$$

Substituting Eq. (18) into Eq. (17) and considering a homogenous dielectric with  $\rho_v = 0$  results in the Laplace's equation:

$$\nabla \cdot \nabla U = 0 \tag{19}$$

Eq. (19) has to be transformed into an energy functional form that relates directly to the energy of the system in order to be used in FEM. This function can be written for an element  $\alpha$  as:

$$F_\alpha = \int_\alpha \frac{1}{2} \epsilon_0 \epsilon_r E^2 d\alpha \tag{20}$$

with units of  $\text{V}^2/\text{m}^2$  for a one-dimensional domain, for example.

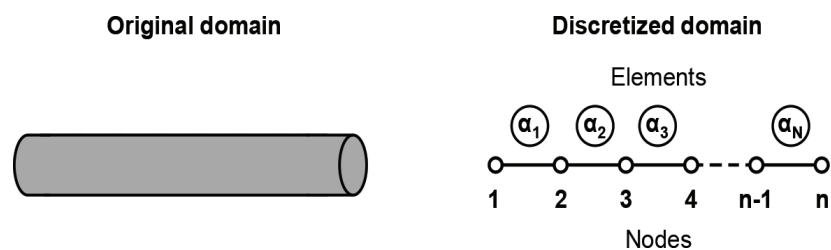


**Figure 5.** Example of one-dimensional domain discretization.

The function gives the voltage distribution that satisfies the governing partial equation when differentiated with respect to  $U$  and equaled to zero. Thus, the change in the global function due to the change in the voltage of node  $i$  is:

$$\frac{\partial F}{\partial U_i} = \sum_{\alpha} \frac{\partial F_{\alpha}}{\partial U_i} \quad (21)$$

where the summation represents the contribution from all elements associated with  $U_i$  or all the elements connected to node  $i$ . These derivatives are equaled to zero resulting in a group of simultaneous equations arranged in matrix form as:

$$[S_i]\{U_i\} = 0 \quad (22)$$

where  $[S_t]_{n \times n}$  is the stiffness matrix whose terms are defined by geometric parameters of the nodes and material properties.  $\{U_i\}_{n \times 1}$  is a column matrix of voltages, which are the unknowns to be solved. Additionally, the boundary values of voltage associated to some of the nodes are applied to this matrix. After the determination of the voltage distribution, the electric field can be obtained by numerically solving Eq. (18).

As it can be noticed, the assumptions made in the original analytical problem for the FEM strongly affect the results. Thereby, the results provided by the simulation have to be validated to ensure their accuracy. To do so, these results are compared to the ones of an analytical model derived for specific conditions as previously presented. Analytical results of electric field from Eqs. (4) and (11) are taken for, respectively, the cylindrical and hemispheric regions as references for the simulation whose parameters of interest are the order of the shape functions and the mesh refinement.

It is worth to mention that the dielectric geometry has a longitudinal axis-symmetry, which implies that the unknown values do not change along the azimuthal axis and thus only a transversal plan needs to be modeled in FEM and the rest of the solution can be extrapolated. **Figure 6** shows the structure modeled around its axis of symmetry for  $a = 18.4 \text{ mm}$  (inner radius) and  $b = 50 \text{ mm}$  (outer radius) in both cylindrical and hemispheric regions. Additionally, voltage boundary conditions were the same as the ones used for the analytical model. Electric field values were extracted along paths P<sub>1</sub>-P<sub>2</sub> and P<sub>3</sub>-P<sub>4</sub>, respectively, in the cylindrical and hemispheric regions.

As a default, COMSOL uses a second order shape function in order to improve the results' accuracy. This choice seems to be adequate as the analytical results showed that the radial variation of the electric field follows a quadratic pattern. However, a mesh convergence study is still needed in order to minimize domain discretization effects on the results. In this procedure, the mesh is successively refined and the values of interest are compared to a reference. **Figure 7** shows the meshes evaluated.

**Figures 8** and **9** show the comparison of analytical results given by Eqs. (4) and (11) with numerical results for three mesh refinements using quadratic shape functions, respectively, for the cylindrical and hemispheric regions. The electric field results obtained by the simulations presented good agreement with the analytical results indicating that quadratic shape functions

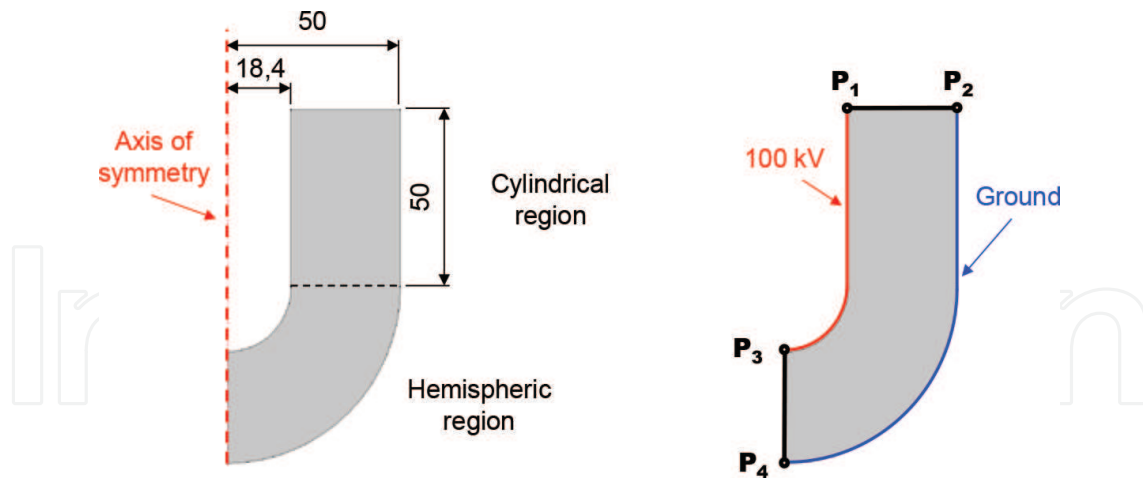


**Figure 6.** Voltage sensor modeled considering its axis of symmetry, voltage boundary conditions and paths of interest for the validation (dimensions in millimeters).

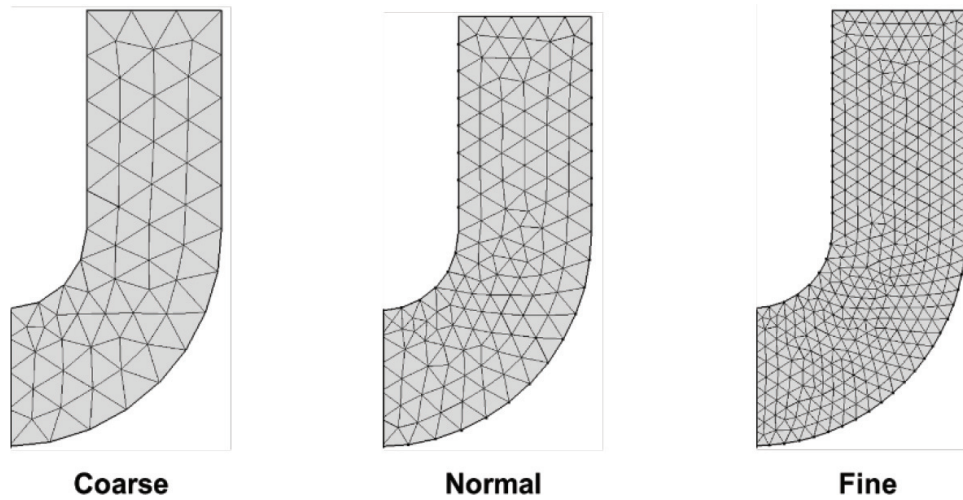


**Figure 7.** Meshes used for the mesh convergence study.

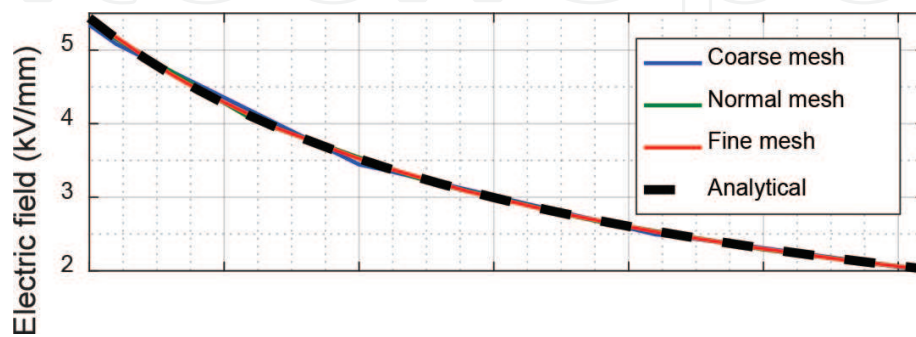


**Figure 8.** Cylindrical region—comparison of analytical and numerical electric fields for mesh selection.

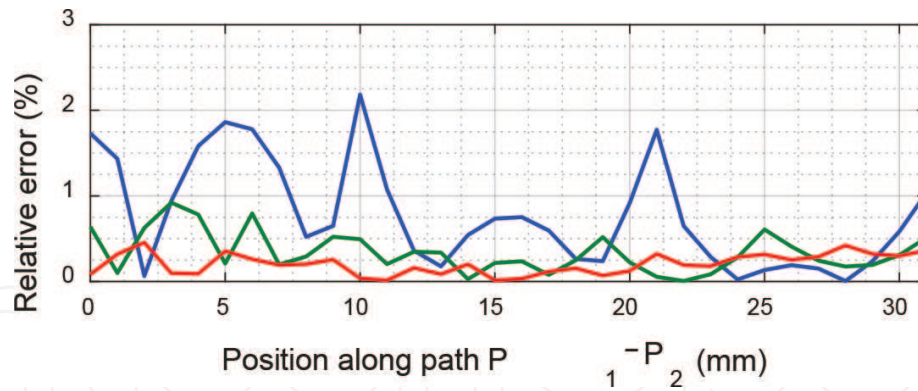


Figure 9. Hemispheric region—comparison of analytical and numerical electric fields for mesh selection.

Numerical (pF)	Analytical (pF)	Difference (%)
Coarse mesh	16.812	0.500
Normal mesh	16.810	16.728
Fine mesh	16.809	0.482

Table 1. Analytical and numerical capacitance values.

are indeed a good choice. In addition, it can be seen that mesh refinement led to a better solution field as the relative error computed using the analytical values as reference decreased. Besides, the duration of the simulations for the three cases did not increase significantly with the last case taking about 1 s. The computer used was a workstation with an Intel(R) Core™ i7–4790 3.60 GHz CPU and 16 GB of RAM.

Finally, another way to validate the simulations is to compute capacitance values from the simulations by numerical integration of the electrical flux along the inner surface in which 100 kV was applied. These values are compared with the analytical one described by Eq. (14) as shown in Table 1.

Since the model related to the fine mesh provided electric field distributions that best agreed with the analytical results in both cylindrical and hemispheric regions of the voltage sensor, and get a capacitance value that closest matched with Eq. (14), this model was successfully validated and will be used in the case study presented below.

## 5. A case study using COMSOL

As explained in Section 3, the modification of the cylinder termination of the central electrode, passing from a flat half ellipsoid of revolution to a stretched half ellipsoid of revolution, aims to optimize the electric field on this region. Therefore, the optimum geometry of the ellipsoid could be obtained through a parametric study, as shown in Figure 10. Varying only the vertical semi-axis ( $v$ ) and setting the horizontal semi-axis ( $h$ ) constant, the geometry of the cylinder

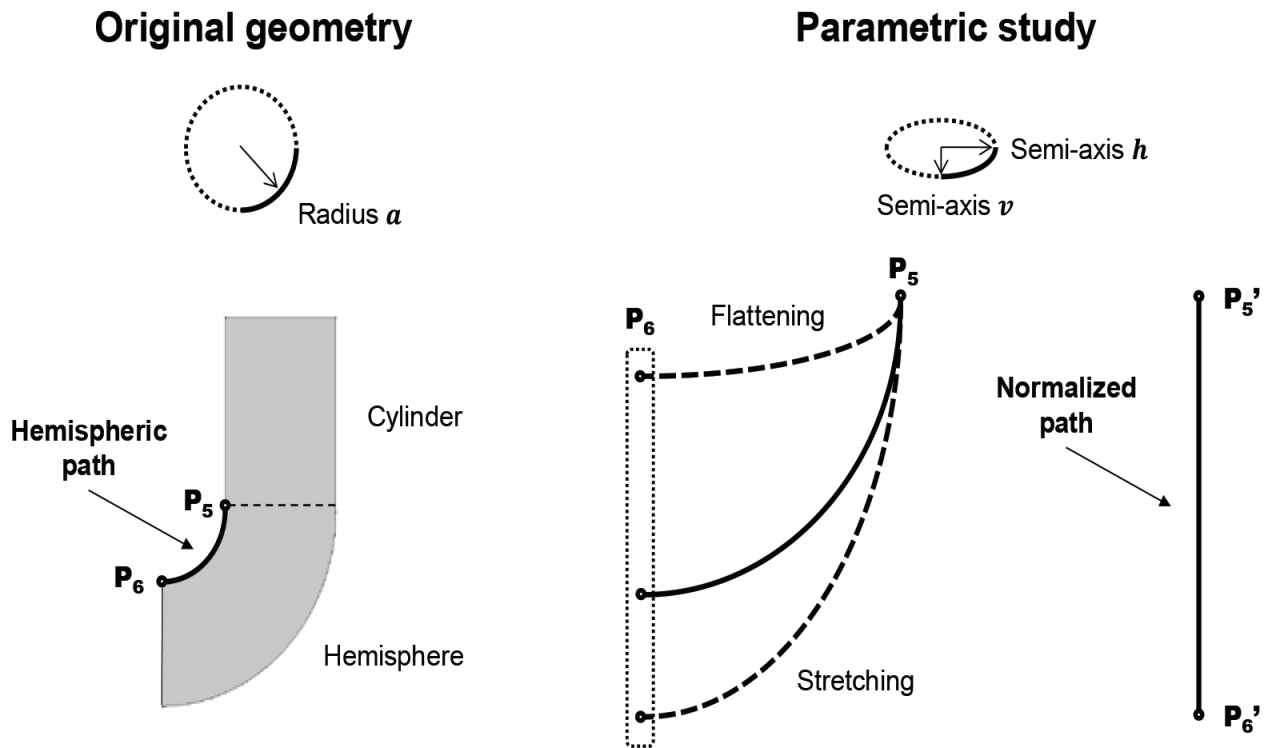


**Figure 10.** Illustration of parametric study based on the geometric modification of the hemispheric region.

termination shall change from a flat geometry up to a stretched geometry between points  $P_5$  (region next to transition from cylindrical region to the elliptic region) and  $P_6$  (region at the tip of centre electrode).

From the simulation of the electric field for different values of semi-axis  $v$ , it is verified that for small values of semi-axis  $v$ , the electric field is more concentrated on the edges and assumes large values in the transition region from cylinder region to elliptic region presenting irregular distribution, as shown in **Figure 11**. Similarly, an irregular distribution is observed for large values of semi-axis  $v$ , but with more concentration of electric field at the tip of the central electrode. On the other hand, for values of semi-axis  $v$  near the hemispheric geometry of radius  $a$ , a better electric field distribution for the entire surface is observed with a minimum concentration. This result shows that the investigation for the optimum condition should be concentrated around the hemispheric geometry.

To do so, a normalized path between points  $P_5'$  and  $P_6'$  is used in order to provide a better visualization for the distribution of electric field norm for different geometries of the central electrode, as shown in **Figure 10**. As an illustration of this procedure, considering two distinct geometries having different lengths and shapes of original paths  $P_5$ - $P_6$ , such as the flat and stretched cases of **Figure 11**, their electric field can be directly compared through the path normalization proposed. This is performed in **Figure 12** where the flat geometry shows an electric field concentration close to point  $P_5'$  while for the stretched geometry the concentration is observed at the tip (point  $P_6'$ ), as expected. Additionally, the hemispheric geometry produces a small electric field norm variation along the trajectory between points  $P_5'$  and  $P_6'$ . This

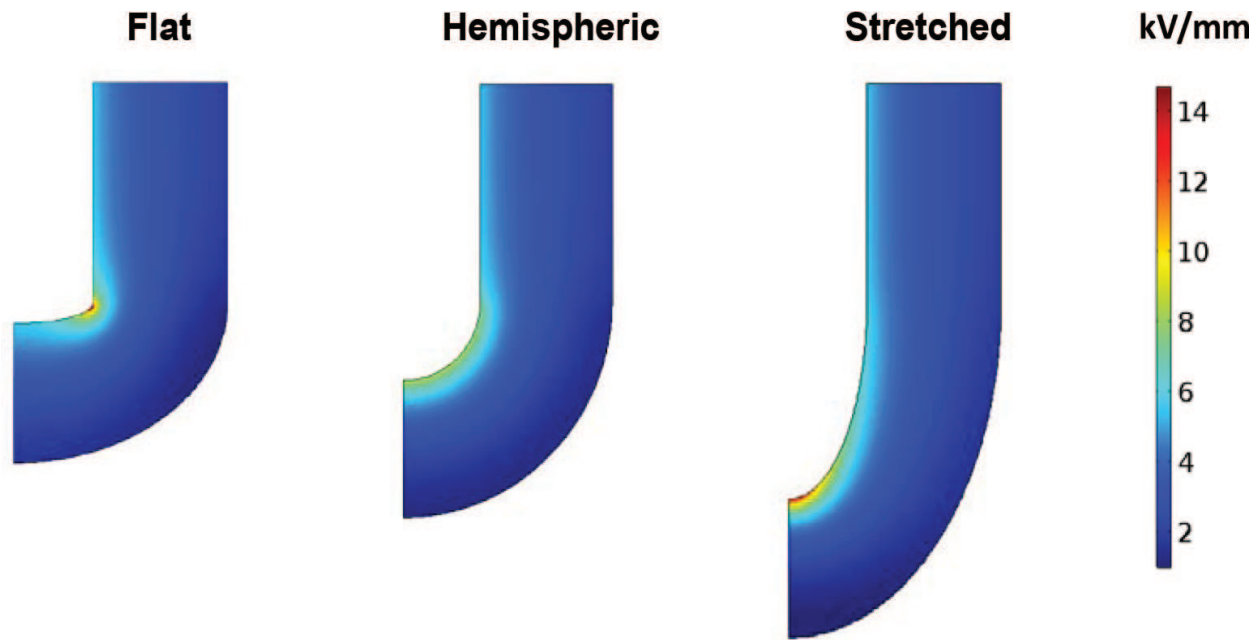


Figure 11. Electric field distribution for three geometries.

emphasizes that the best geometry for the central electrode in terms of electric field distribution must be close to the hemispheric geometry.

Therefore, this work has been focused on parametric studies around the hemispheric geometry with variations in the value of the semi-axis  $v$  of the central electrode. Eleven cases were simulated with a step of 0.2 mm being five cases below 18.5 mm (tip flattening) and five cases above 18.5 mm (tip stretching), as shown in **Figure 13**. It is important to note the effect of geometric modification on electric field norm along normalized path  $P_5'-P_6'$ . As an example, the response curve for the flattening geometry has bigger values of electric field close to the point  $P_5'$  and lower values close to the point  $P_6'$ . Also, these curves indicate the existence of a case whose maximum electric field value along  $E'-F'$  path is the smaller one among the other curves, making it a candidate for the optimum condition.

**Figure 14** presents the maximum electric field norm along the normalized path  $P_5'-P_6'$  for each case presented in **Figure 13**. The existence of an optimum condition is evidenced by the trend in the results provided by the simulated cases. The exact value of the semi-axis  $v$  for this optimum condition is obtained through interpolation, leading to an optimum *value* of 17.5 mm.

A new parametric study was performed in order to confirm the best condition found. Three cases around the optimum semi-axis  $v$  of 17.5 mm were simulated with a smaller step of 0.1 mm. **Figure 15** shows these results indicating that the solution for  $v = 17.5$  mm is indeed the optimum solution since it ensures the lowest electric field norm when the whole normalized path  $P_5'-P_6'$  is considered. Another form of analysis is to compute a relative percent difference taking the electric field norm from the cylindrical region, which is constant for any modifications in the geometry of the hemispheric region, as a reference (5.447 kV/mm). As it

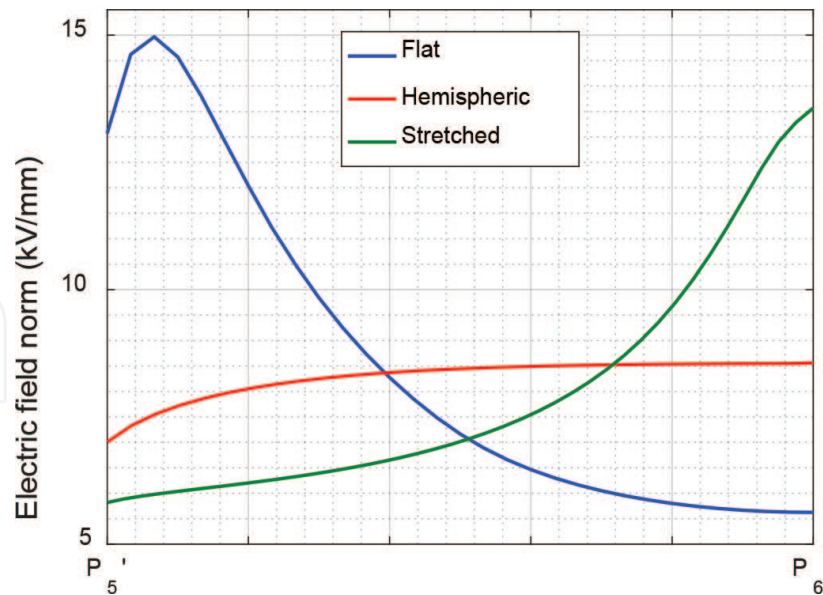


Figure 12. Electric field norm along normalized path  $P_5'-P_6'$  for three geometries.

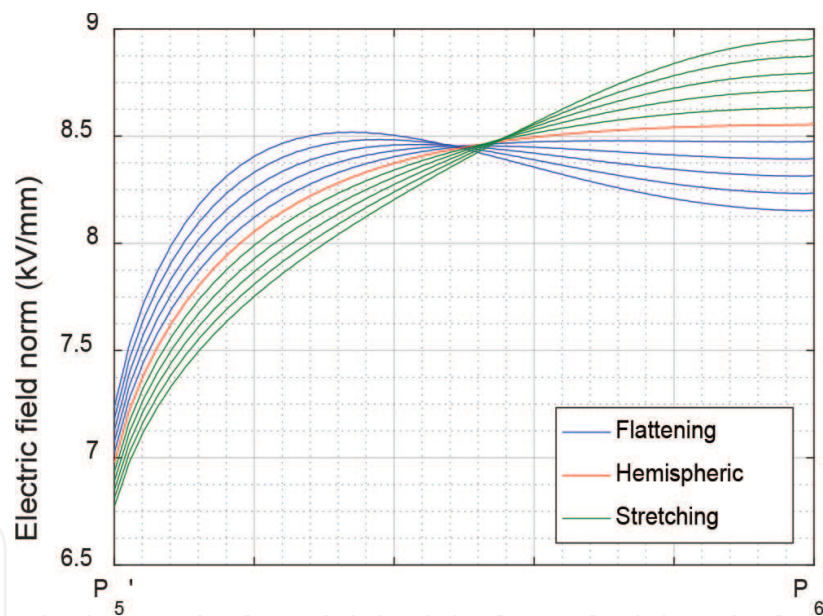


Figure 13. Effect of tip deformation on electric field norm along normalized path  $P_5'-P_6'$ .

can be seen, again the optimum condition curve presents smaller values than the other curves when the whole normalized path  $P_5'-P_6'$  is considered.

This conclusion is supported by an extension of the last parametric study, as shown in the **Figure 16**, where 21 different values around 17.5 mm with a step of 0.1 mm for the semi-axis  $v$  were computed. The relative difference metric was calculated for the maximum value of each electric field norm distribution evidencing the optimum condition of 17.5 mm, as expected.

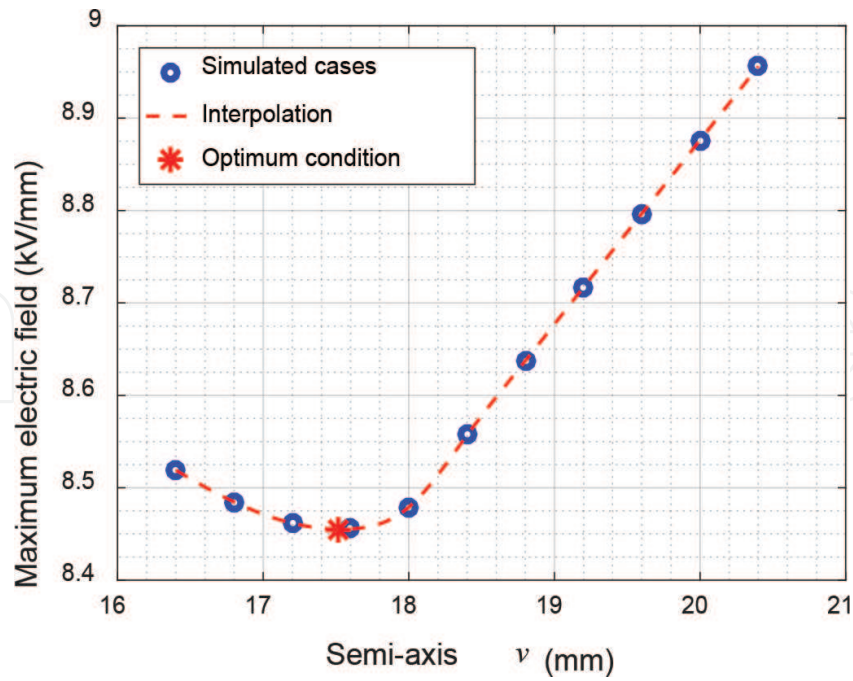


Figure 14. Interpolation of results for optimum condition.

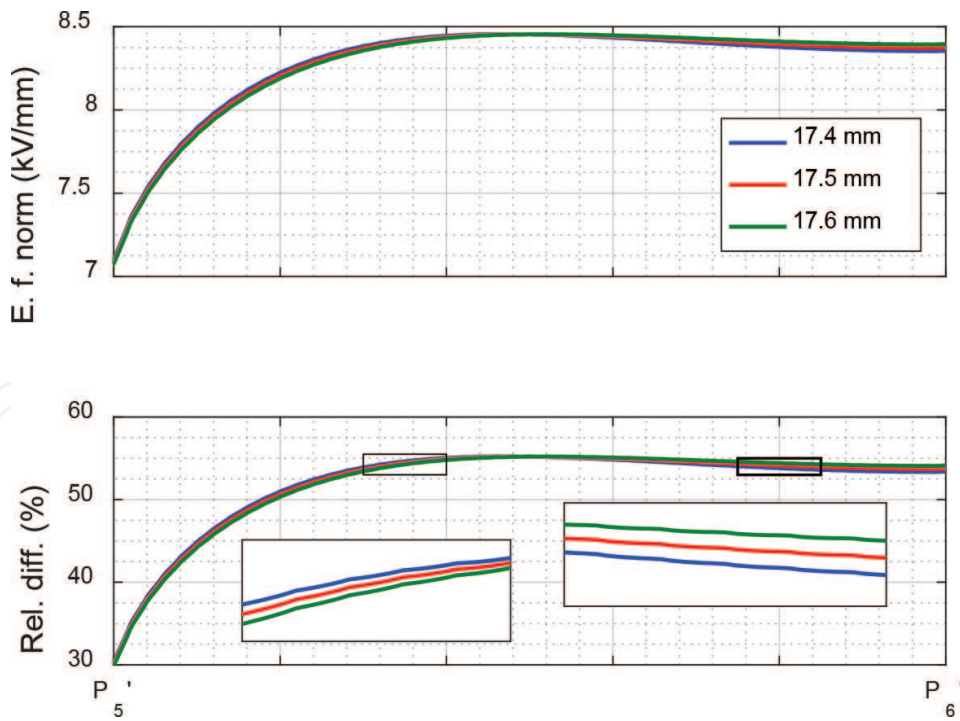
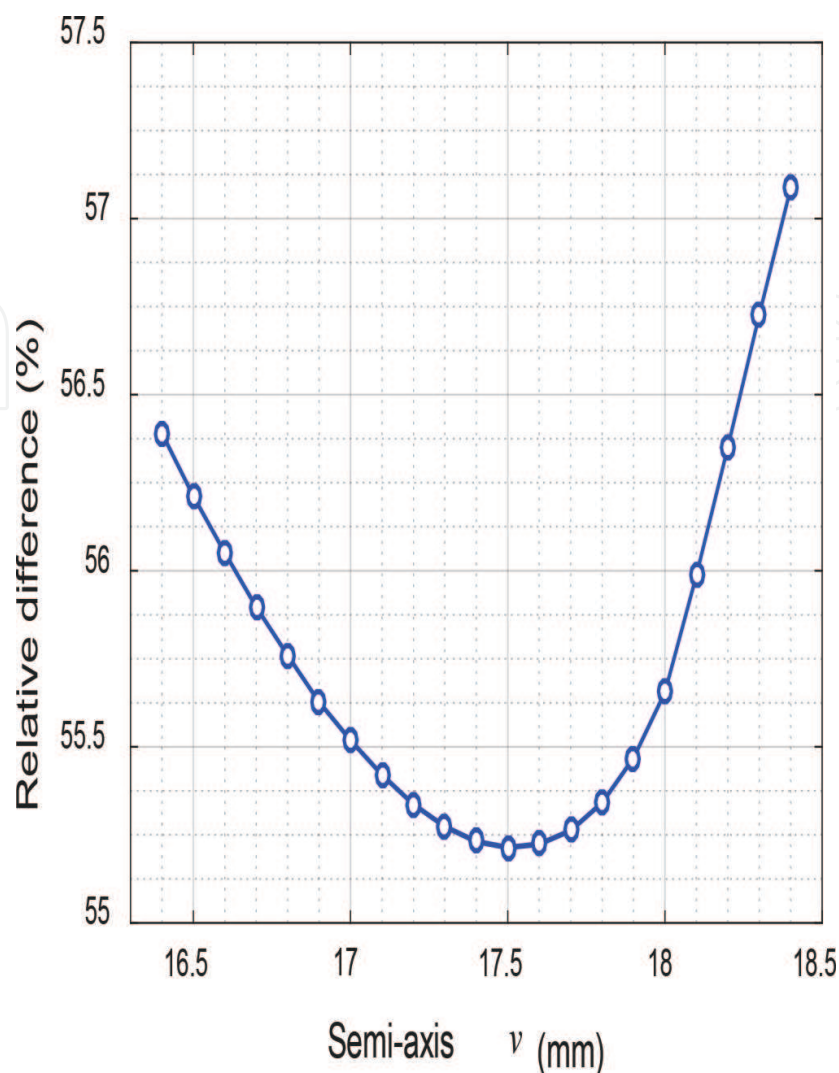


Figure 15. Electric field norm and relative difference metric along normalized path  $P_5'$ - $P_6'$  for optimum condition verification.



**Figure 16.** Relative difference of maximum electric field norm considering cylindrical region as reference.

Another conclusion is that, for this optimum geometry, a reduction of approximately 1.5% in the maximum electric field is achieved when compared to the hemispheric geometry. This improvement is strategic to ensure the safe operation of the sensor since partial discharge is a localized phenomenon influenced by electric field concentration. In a real scenario, because of imperfections in the dielectric due to the manufacturing process, such as air bubbles, a lightning impulse of 100 kV can lead to local discharges in points of high-electric field concentration, which will cause the failure of the sensor.

Finally, **Figure 17** shows the  $C_2$  capacitance variation for a wide-range of values of semi-axis  $v$  covering the geometries presented in **Figure 11**. It is possible to see that the value of  $C_2$  for the optimum condition is very close to the ones shown in **Table 1** since the geometry of the optimum condition is very close to a hemisphere. In addition, the range of capacitance values obtained is compatible to the design of the capacitive divider.

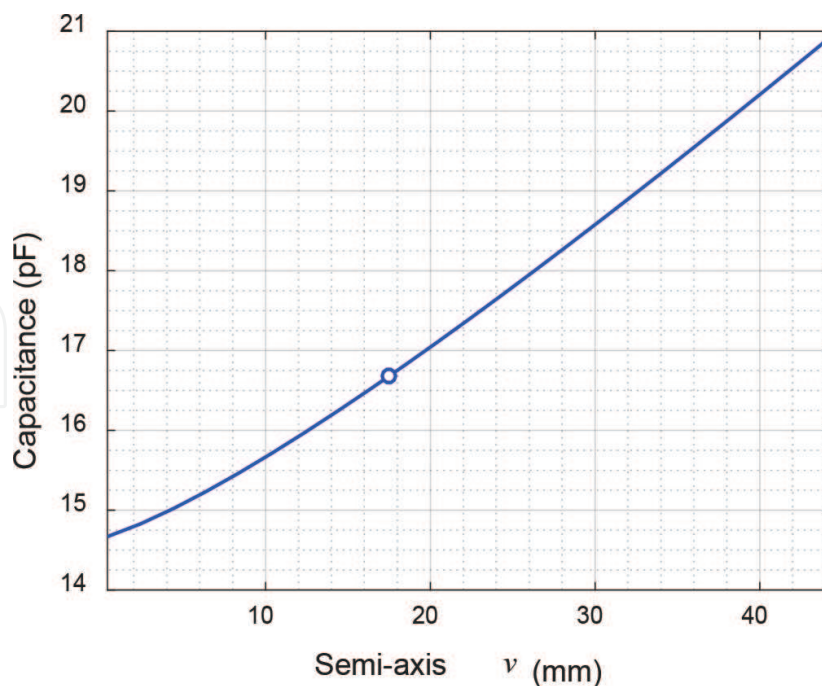


Figure 17. Capacitance values  $C_2$  for different values of semi-axis  $v$ . The mark indicates optimized electric field condition.

## 6. Conclusion

A rigorous capacitor design is necessary for MV sensors when capacitive divider is used to obtain a voltage sample. This is due to safety aspects regarding to the technician activities and some environmental effects that can influence their performance, such as temperature, pressure and wind. In addition, external elements in the vicinity of the sensor can alter the electric field acting inside of it.

The basic structure adopted for the voltage sensor is composed of two-coaxial cylinders terminated in a hemisphere, which simplifies the practical construction of the capacitor. Although, this work demonstrated that the geometry of the electrode termination should be different of a hemisphere in order to minimize the electric field distribution in this region.

This conclusion was based in finite-element studies developed in COMSOL software. The first one, considered a hemispheric electrode termination of 18.4 mm of radius and was compared to an analytical model for validation purposes. Next, a parametric study was developed, in which the termination was changed from a flat to a stretched geometry, to obtain the optimum condition. The electric field distribution along the termination for this condition was compared to a reference value extracted from the cylindrical region (5.447 kV/mm). The result is that the optimum geometry is slightly flatter than a hemisphere having a semi-axis  $v$  equals 17.5 mm.

Additionally, the electric field distributions of the optimum and the hemispheric geometries were compared evidencing a magnitude reduction of approximately 1.5%. This improvement is strategic to ensure the safe operation of the sensor since partial discharge is a localized phenomenon influenced by electric field concentration. In a real scenario, because of

imperfections in the dielectric due to manufacturing process imprecision, such as air bubbles, a lightning impulse of 100 kV can lead to local discharges in points of high electric field concentration, which will cause the failure of the sensor.

## Acknowledgements

The authors wish to thank their colleague Celio Fonseca Barbosa.

This work was funded by FINEP (Brazilian Innovation Agency) grant number 0115002800 0407/14.

CNPq (National Counsel of Technological and Scientific Development) sponsors the author Joao B. Rosolem under scholarship DT.

## Conflict of interest

The authors declare no conflict of interest.

## Author details

Sender Rocha dos Santos, Rodrigo Peres, Wagner Francisco Rezende Cano and Joao Batista Rosolem\*

\*Address all correspondence to: [rosolem@cpqd.com.br](mailto:rosolem@cpqd.com.br)

CPqD – Research and Development Center in Telecommunications, Campinas, SP, Brazil

## References

- [1] Colak I. Introduction to smart grid. In: Proceedings of the International Smart Grid Workshop and Certificate Program (ISGWCP); Istanbul; 2016. pp. 1-5. DOI: 10.1109/ISGWCP.2016.7548265
- [2] Parker DM, McCollough ND. Medium-voltage sensors for the smart grid: Lessons learned. In: Proceedings of the IEEE Power and Energy Society General Meeting; San Diego; 2011. pp. 1-7. DOI: 10.1109/PES.2011.6039775
- [3] International Electrotechnical Commission. IEC 61000-4-30:2015 - Electromagnetic Compatibility (EMC)—Part 4-30: Testing and AQ01 25 Measurement Techniques - Power Quality Measurement Methods. Geneva, Switzerland; 2015

- [4] International Electrotechnical Commission. IEC 61000-4-7:2002+AMD1:2008 CSV-Electromagnetic Compatibility (EMC)—Part 4-7: Testing and Measurement Techniques—General Guide on Harmonics and Interharmonics Measurements and Instrumentation, for Power Supply Systems and Equipment Connected Thereto. Geneva, Switzerland; 2008
- [5] Lim Y, Kim H-M, Kang S. A design of wireless sensor networks for a power quality monitoring system. *Sensors*. 2010;**10**:9712-9725. DOI: 10.3390/s101109712
- [6] Zavoda F, Yakymyshyn C. Sensors for smart grids. In: Proceedings of the Third International Conference on Smart Grids, Green Communications and IT Energy-Aware Technologies (ENERGY 2013); Lisbon; 24–29 March 2013. pp. 83-88
- [7] DeMaria L, Pistoni NC. An optical approach for monitoring electrical parameters in a distribution network. In: Proceedings of the XVIII AISEM Annual Conference: Trento; 2015. pp. 1-4. DOI: 10.1109/AISEM.2015.7066792
- [8] Štefanka M. Application of sensors and digitalization based on IEC 61850 in medium voltage networks and switchgears [thesis]. Brno: Brno University of Technology, Faculty of Electrical Engineering and Communication; 2016
- [9] Aurilio G, Crotti G, Gallo D, Giordano D, Landi C, Luiso M. MV divider with fiber optic insulation. In: Proceedings of the IEEE International Workshop on Applied Measurements for Power Systems (AMPS); Aachen; 2013. pp. 1-6. DOI: 10.1109/AMPS.2013.6656216
- [10] Sevlian R, Rajagopal R. Actively calibrated line mountable capacitive voltage transducer for power systems applications. *IEEE Transactions on Smart Grid*. 2016;**99**:1-1. DOI: 10.1109/TSG.2016.2643636
- [11] Moreno MVR, Robles G, Albarracín R, Rey JA, Tarifa JMM. Study on the self-integration of a Rogowski coil used in the measurement of partial discharges pulses. *Electrical Engineering*. 2016;**99**:1-10
- [12] International Electrotechnical Commission. IEC 60038:2009 – IEC Standard Voltages. Geneva, Switzerland; 2009
- [13] International Electrotechnical Commission. High Voltage Test Techniques—Part I: General Definitions and Test Requirements. Geneva, Switzerland; 2010
- [14] Siada AA. Power Transformer Condition Monitoring and Diagnosis. Chapter 2: Power Transformer Condition Monitoring and Diagnosis: Concepts and Challenges. Albarracín R, Robles G, Ardila-Rey JA, Cavallini A, Passaglia R. Pagination: c; 2018. 300pp. ISBN: 978-1-78561-254-1
- [15] Kreuger FH. Partial Discharge Detection in High-Voltage Equipment. Oxford, UK: Butterworth-Heinemann Ltd; 1989
- [16] Boggs SA. Partial discharge. III. Cavity-induced PD in solid dielectrics. *Electrical Insulation Magazine IEEE*. 1990;**6**(November(6)):11-16. DOI: 10.1109/57.63094 ISSN 0883-7554

- [17] IEC-60270. High-Voltage Test Techniques—Partial Discharge Measurements. 3rd ed. New Delhi, India: IEC; 2000
- [18] Jardine AK, Lin D, Banjevic D. A review on machinery diagnostics and prognostics implementing condition-based maintenance. *Mechanical Systems and Signal Processing*. 2006;**20**:1483-1510. DOI: 10.1016/j.ymsp.2005.09.012
- [19] Gill P. Electrical power equipment maintenance and testing. In: *Power Engineering (Willis)*. 2nd ed. Boca Raton, FL, USA: Taylor & Francis; 2008
- [20] Barbosa CF. Horizontal electric field in the vicinity of structures hit by lightning. *Atmosphere*. 2016;**7**:115-130. DOI: 10.3390/atmos7090115
- [21] Halliday D, Resnick R, Walker J. *Fundamentals of Physics: Electromagnetism*. 7th ed. Vol. 3. USA: Wiley International Edition; 2005
- [22] Haque SM, Rey JAA, Masúd AA, Umar Y, Albarracín R. Electrical Properties of Different Polymeric Materials and their Applications: The Influence of Electric Field, Polymer Dielectrics Boxue Du, IntechOpen; 2017. DOI: 10.5772/67091
- [23] DIN 53481. Testing of Electrical Insulating Materials; Determination of the Electrical Breakdown Voltage and Electric Strength. Berlin, Germany: German Institute for Standardization; 1974
- [24] Baker AE, Preston TW, Sturgess JP. Numerical analysis of electrical fields in high voltage equipment (*Energy Engineering*, 2004). *Advances in High Voltage Engineering*, Chap. 11, pp. 511-544, IET Digital Library. DOI: 10.1049/PBPO040E\_ch11
- [25] Zepu W, Nelson JK, Hillborg H, Zhao S, Shadler LS. Dielectric constant and breakdown strength of polymer composites with high aspect ratio fillers studied by finite element models. *Composites Science and Technology*. 2013;**76**:7629-7636. DOI: 10.1016/j.compscitech.2012.12.014
- [26] Christen T. Nonstandard high-voltage electric insulation models. In: *Proceedings of the COMSOL Conference Europe*; Milan; 2012
- [27] Pedersen A et al. Streamer inception and propagation models for designing air insulated power devices. In: *Proceedings of the CEIDP Conference*; Virginia Beach: Material; 2009. DOI: 10.1109/CEIDP.2009.5377740
- [28] Christen T. Streamer inception and propagation from electric field simulations. In: *Proceedings of the Scientific Computing in Electrical Engineering (SCEE)*; 11–14 September; Zürich; 2012

